

# Supercritical CO<sub>2</sub> extraction of porogen phase: An alternative route to nanoporous dielectrics

J.A. Lubguban and S. Gangopadhyay<sup>a)</sup>

*Department of Electrical and Computer Engineering, University of Missouri, Columbia, Missouri 65211*

B. Lahlouh, T. Rajagopalan, and N. Biswas

*Physics Department, Texas Tech University, Lubbock, Texas 79409*

J. Sun, D.H. Huang, and S.L. Simon

*Chemical Engineering Department, Texas Tech University, Lubbock, Texas 79409*

A. Mallikarjunan

*Center for Integrated Electronics, Rensselaer Polytechnic Institute, Troy, New York 12180*

H-C. Kim, J. Hedstrom, W. Volksen, and R.D. Miller

*IBM Almaden Research Center, San Jose, California 95120*

M.F. Toney

*SSL, Stanford Linear Accelerator Center, Menlo Park, California 94025*

(Received 6 April 2004; accepted 12 July 2004)

We present a supercritical CO<sub>2</sub> (SCCO<sub>2</sub>) process for the preparation of nanoporous organosilicate thin films for ultralow dielectric constant materials. The porous structure was generated by SCCO<sub>2</sub> extraction of a sacrificial poly(propylene glycol) (PPG) from a nanohybrid film, where the nanoscopic domains of PPG porogen are entrapped within the crosslinked poly(methylsilsesquioxane) (PMSSQ) matrix. As a comparison, porous structures generated by both the usual thermal decomposition (at approximately 450 °C) and by a SCCO<sub>2</sub> process for 25 and 55 wt% porogen loadings were evaluated. It is found that the SCCO<sub>2</sub> process is effective in removing the porogen phase at relatively low temperatures (<200 °C) through diffusion of the supercritical fluid into the phase-separated nanohybrids and selective extraction of the porogen phase. Pore morphologies generated from the two methods are compared from representative three-dimensional (3D) images built from small-angle x-ray scattering (SAXS) data.

## I. INTRODUCTION

The continuing demand for higher performance in ultra-large-scale integration has led to shrinking device dimensions and a concomitant increase in the number of components on a single chip.<sup>1</sup> For example, when Intel introduced its microprocessor in 1971, the number of transistors on a single chip was 2250 whereas 42 million transistors were packed on a single chip in 2000, resulting both in much faster data processing and much lower cost per transistor.<sup>2</sup> This increased performance is largely attributed to the decrease in intrinsic gate delay in transistors with device scaling. However, as feature sizes decrease further to submicron levels, the interconnect resistance-capacitance (RC) delay at the back-end-of-the-line (BEOL) can no longer be ignored. The BEOL, consisting mainly of metal wiring and dielectric material, is

responsible for carrying electrical power and for distributing clock signals between components during device operation. The RC delay increases exponentially as feature size decreases below 1 μm.<sup>1</sup> Further complicating the problem is increasing power dissipation and crosstalk noise.<sup>3</sup> The successful implementation of Cu as replacement for Al has resulted in a decrease in RC delay by as much as 37% due mainly to its lower resistivity. Further significant reductions require the replacement of the standard dielectric material (SiO<sub>2</sub>) with a lower dielectric constant ( $k$ ) material. For example, substitution of SiO<sub>2</sub> ( $k = 4.0$ ) with a material with  $k = 2.0$  will reduce the delay by 50%. The International Technology Roadmap for Semiconductors (ITRS), which has projected the overall technology requirements since 1994, has suggested that for technology nodes <45 nm, dielectrics with  $k < 2.1$  are needed.<sup>4</sup>

Research has produced large numbers of materials with  $k$ -values ranging from 1.1 to 3.0 and deposited mostly via spin-on (SOD) or chemical vapor deposition

<sup>a)</sup>Address all correspondence to this author.

e-mail:gangopadhyays@missouri.edu

DOI: 10.1557/JMR.2004.0413

(CVD).<sup>1</sup> However, most of these materials candidates do not fully satisfy the rigorous mechanical, chemical, electrical, and thermal requirements for device integration. Fluorinated silicon dioxide (FSG) films with  $k = 3.2$  to  $3.6$  have been successfully integrated at the 180 nm node.<sup>4</sup> Likewise, organosilicates with dielectric constant of 2.6–2.8 deposited by current CVD tools have also been introduced and developed with Cu technology.<sup>3</sup> However technology nodes below 100 nm continue to present a serious integration and characterization challenge for new materials.

Since a limited number of fully dense materials satisfy  $k < 2.5$  requirements, research has been focused on the preparation of porous films.<sup>3</sup> The ability to tailor the degree of porosity and the size and shape of pores offers versatility and extendibility which makes porous films attractive low- $k$  candidates. Although, porous films can be prepared by either CVD or SOD, the SOD scheme is by far the most widely used.<sup>3</sup> Some of the methods for preparation of porous dielectrics include nanohybrid techniques, block copolymers, templated self-assembly, solvent-as-porogen approaches, and sol-gel techniques.<sup>3</sup> Of particular interest is the nanohybrid method, or so-called sacrificial porogen approach, which generates pores by removal of thermally degradable organic macromolecules (porogens) from the nanohybrid comprised of the porogen and a crosslinked matrix. Possible porogens include amphiphiles, micelles, lyotropic phases, polymeric spheres, and assemblies of polymeric spheres, all of which provide versatility and control not only the pore size and size distribution but also the pore morphology.<sup>5</sup> In addition, the degree of porosity can be adjusted by simply varying the mixing ratio of matrix and template precursors. The morphology of the porous films is a crucial factor affecting the performance of the film. Generally, closed pores in the matrix are desirable because pore interconnectivity may result in low mechanical strength, low thermal conductivity, and low breakdown voltage. Highly interconnected pores may also allow contaminants to diffuse between structures, possibly resulting in electrical shorts. Furthermore, pores should be uniformly distributed in the films to provide isotropic dielectric constant values.

A typical process flow of the nanohybrid method using nucleation and growth porogens can be described as follows. The first step is the choice of suitable matrix material, porogen, and mutual solvent. The precursor mixture is spin coated on the substrates, followed by soft baking (100 °C) to expel the solvent. During the curing period (200–250 °C), the matrix crosslinks and the porogen phase separates into nanoscopic domains. Finally, removal of the porogen phase occurs by thermal decomposition at relatively higher temperatures (350–450 °C). In this step, the matrix is further cured. The usual method of creating pores is thermal decomposition of porogen

phase. The inherent disadvantage with this method is that process temperature window can be narrow because the thermal decomposition of porogens must occur substantially below the glass transition ( $T_g$ ) of the matrix to prevent collapse of porous structure. Since many organic polymers have relatively low  $T_g$ s compared to degradation temperatures of porogens, this constraint can lead to incomplete porogen decomposition often resulting in char residue.

To address these issues, supercritical CO<sub>2</sub> (SCCO<sub>2</sub>) is presented as an alternative to thermal decomposition of the porogen phase. The idea is for SCCO<sub>2</sub> to diffuse into the film, dissolve, and remove the porogens from the matrix via venting. Here, the porogen molecules are not decomposed but rather selectively extracted from the crosslinked matrix. SCCO<sub>2</sub>, i.e., CO<sub>2</sub> at pressures and temperatures above 1050 psi and 31 °C, has gaslike viscosity and diffusivity and has liquidlike solvating strength. These properties allow the possibility of extraction at lower temperatures than for the thermal annealing process. SCCO<sub>2</sub> has been extensively used in industrial and analytical processes and waste detoxification<sup>6</sup> and has recently found interesting applications in semiconductors. Researchers at Los Alamos National Laboratory (Los Alamos, NM) have successfully removed photoresist using SCCO<sub>2</sub> with minimal use of solvent.<sup>7</sup> Here, there is no doubt about its advantageous cost impact to the semiconductor industry and its positive environmental effect due to reduction of toxic solvents in photoresist stripping.<sup>8</sup> SCCO<sub>2</sub> is also a promising cleaning technique for high aspect ratio vias and trenches and one study reported that SCCO<sub>2</sub> also increased the mechanical strength of porous materials.<sup>9</sup> In a previous paper, we reported the ability of SCCO<sub>2</sub> to dissolve low molecular weight and loosely bonded species in films prepared by plasma-enhanced CVD.<sup>10</sup> Supercritical CO<sub>2</sub> has been used effectively for the extraction and isolation of organic and inorganic compounds, including removal of hazardous organic waste from contaminated soil,<sup>11,12</sup> fractionation of natural oils,<sup>13–16</sup> and extraction of biomolecules,<sup>17</sup> metal ions,<sup>18–21</sup> and polymerization catalysts.<sup>22</sup> We believe that extraction of porogens in a hybrid inorganic–organic film for semiconductor applications is unique and applied for the first time by our group.<sup>23,24</sup>

## II. EXPERIMENTAL

### A. Preparation of nanoporous films

An organosilicate, poly(methylsilsesquioxane) (PMSSQ) having an empirical formula  $(\text{CH}_3\text{-SiO}_{1.5})_n$ , was chosen as a matrix due to its inherently low value of  $k$  (2.85), low moisture uptake, and excellent thermal stability up to 500 °C.<sup>25</sup> Poly(propylene glycol)

{PPG; [-CH(CH<sub>3</sub>)CH<sub>2</sub>O-]<sub>n</sub>} from Bayer Polymers (Pittsburgh, PA) (Acclaim™) with a linear structure,  $M_n = 20,000$  g/mol and polydispersity index (PDI) = 1.05, is chosen as a porogen material. Appropriate quantities of PPG and PMSSQ were dissolved in propylene glycol methyl ether acetate (PGMEA) and the solution was loaded into a disposable syringe before passing through a 0.2- $\mu\text{m}$  polytetrafluoroethylene (PTFE) filter and onto silicon substrates. After spin coating at 3000 rpm for 30 s, the samples were heated briefly to 50 °C on a hot plate under nitrogen atmosphere to remove the solvent before curing at 200 °C to produce the phase-separated structure. This curing temperature is still well below the thermal degradation temperature (430 °C) of the porogen in an inert atmosphere. The curing at 200 °C produced films in its hybrid state, where porogens are phase-separated and entrapped in the matrix. The chemistry and crosslinking schemes of PMSSQ is well described in the paper of Baney et. al.<sup>26</sup> whereas the phase separation between the PMSSQ and PPG at this temperature is evident from previous small angle neutron scattering data.<sup>27</sup> The phase separation scheme between inorganic-organic hybrids have been presented in detail by several papers.<sup>28–30</sup> Films with porogen compositions of 25 wt% (OS7525) and 55 wt% (OS4555) were prepared for this study. According to preliminary results from positron annihilation spectroscopy on porous films generated thermally, the former composition is expected to form a nanohybrid with predominantly dispersed porogen morphology while the latter results in an interconnected nanohybrid. For simplicity, the two samples after undergoing phase separation by curing at 200 °C will be referred to as “as-cured.”

## B. Supercritical CO<sub>2</sub> extraction

Figure 1 shows the schematic diagram of the supercritical extraction system. The vessel is of stainless steel 316 and is rated to withstand operating pressures up to 10,000 psi and temperatures up to 200 °C. The cylindrical vessel with inner diameter of 2.5 cm, inner depth of 12.7 cm, and outer diameter of 6.3 cm is placed inside an

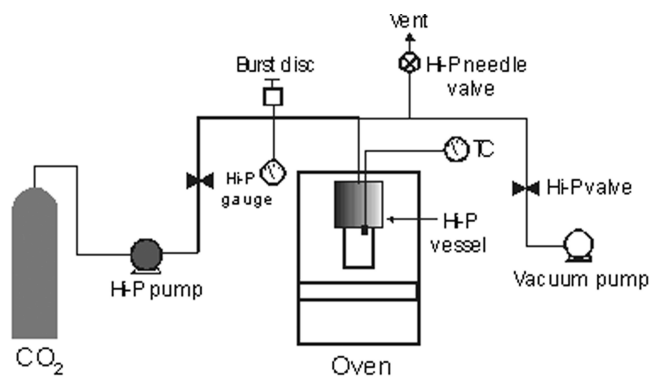


FIG. 1. Schematic diagram of the supercritical CO<sub>2</sub> extraction system.

oven. The temperature inside the vessel is monitored by a thermocouple placed inside a thermo-well that extends 2.5 cm deep. A vacuum pump is fitted to evacuate ambient air before pressurization with CO<sub>2</sub> using air-driven gas booster pumps (Haskel, Burbank, CA). A gauge (Sensotec, Columbus, OH) gives the pressure reading and the pressure in the vessel is controlled by a ball valve installed between the gas booster and extraction vessel. A burst disk is installed for safety. The extraction is done as follows. First, the films were arranged in the substrate holder and placed inside the pressure vessel. The ambient air was then pumped out and the vessel backfilled with CO<sub>2</sub> at approximately 300 psi. The oven temperature was then ramped slowly (4 h to reach 200 °C) to the desired temperature. The vessel was subsequently pressurized isothermally with CO<sub>2</sub> with a purity of 99.99% using the gas boosters driven with 70-psi air pressure. The pressure in the chamber was maintained over the duration of the extraction experiment. The vessel was then depressurized to 500 psi and the temperature was ramped down to 25–30 °C. Depressurization to atmospheric pressure was then completed at this temperature.

## C. Characterization

Fourier transform infrared (FTIR) spectra at the 4000–400 cm<sup>-1</sup> range were recorded using a Perkin-Elmer (Boston, MA) Model 1600 spectrometer with a resolution of 8 cm<sup>-1</sup>. The thickness and refractive index of the samples were measured by a prism coupler (Metricon 2010, Pennington, NJ) and ellipsometer (Rudolph, Flanders, NJ, AutoEL IV). Porosity was estimated using the Claussius–Mossotti equation and was also compared with the Bruggemann effective medium approximation method.<sup>31</sup> For dielectric constant measurements, a metal-insulator-semiconductor structure is fabricated by e-beam evaporation of Ti to form dots with an area of 0.196 mm<sup>2</sup> on top of the films spin-coated on heavily doped silicon substrates. An HP 4275A LCR meter set at a frequency of 10 kHz measured the capacitance for dielectric constant calculation. The microstructure of the samples after extraction was examined using small-angle x-ray scattering (SAXS). The SAXS experiments were performed at the IMM-CAT at the Advanced Photon Source at Argonne National Laboratory (Argonne, IL). The incident x-rays from an undulator were monochromatized with a Ge (111) crystal to an energy of 7.66 keV. Slits confined the incidence beam size to either 100 × 100  $\mu\text{m}$  (high resolution) or 200 × 200  $\mu\text{m}$  (low resolution). An area detector was used with a sample-to-detector distance of either 3290 mm (high resolution) or 550 mm (low resolution). The high and low resolution data sets were merged and the SAXS from the PMSSQ (originating from the ladder structure<sup>32</sup>) was subtracted from the merged data to give the SAXS from the pores.

### III. RESULTS AND DISCUSSION

#### A. FTIR

Figure 2 shows a comparison of the FTIR spectrum of three types of films: PMSSQ, PPG, and PMSSQ + PPG. The dominant absorption for the PMSSQ was observed at 1200–1000 cm<sup>-1</sup> and is attributed to Si–O with caged (1120 cm<sup>-1</sup>) and bridging (1035 cm<sup>-1</sup>) configurations.<sup>33</sup> Si–CH<sub>3</sub> is observed at 1275 cm<sup>-1</sup> and CH<sub>3</sub> asymmetric (2960 cm<sup>-1</sup>) and a very small CH<sub>3</sub> symmetric (2900 cm<sup>-1</sup>) modes are the only bands detected for the CH stretching vibrations (3000–2800).<sup>15</sup> The broad band at 3700–3200 cm<sup>-1</sup> is attributed to both free Si–OH (3650 cm<sup>-1</sup>) and H-bonded OH (3400 cm<sup>-1</sup>) while the absorption band centered at 930 cm<sup>-1</sup> is due to Si–OH bending.<sup>34</sup> The large amount of hydroxyl group is due to the low baking temperature of 50 °C. For the PPG film baked at 50 °C, the strongest vibrations were also observed at 1200–1000 cm<sup>-1</sup> and are attributed to C–O stretching modes similar to alcohols and ethers.<sup>35</sup> In the CH region of the PPG spectrum, the CH<sub>2</sub> asymmetric (2915 cm<sup>-1</sup>) and symmetric (2870 cm<sup>-1</sup>) modes appeared in addition to the CH<sub>3</sub> vibrations found earlier for the PMSSQ film. The OH functionality is also observed. The PMSSQ + PPG spectrum shows the overlapping of the two film spectrum and is consistent with the expected dominant vibrations in the 1200–1000 cm<sup>-1</sup> region. The 200 °C annealing temperature reduces the OH-related peaks drastically. The CH stretching vibrations observed in PMSSQ + PPG are very similar with those of the PPG film. Comparing the three spectra in the CH stretching region, we conclude that all of the CH<sub>2</sub> absorption peaks in PMSSQ + PPG are due solely to the incorporation of PPG in the film. Upon volatilization or extraction of PPG in the PMSSQ film, we expect the spectra of the remaining film will resemble that of PMSSQ.

Figure 3 depicts the changes in the infrared absorption bands for the hybrid OS7525 (closed pore morphology, as shown by SAXS below) film in the OH and CH

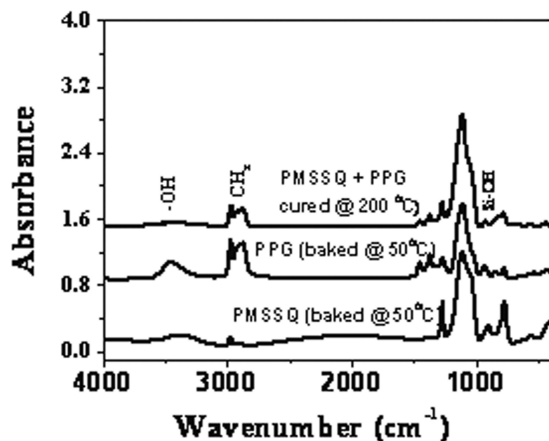


FIG. 2. FTIR spectra of PMSSQ, PPG, and PMSSQ + PPG.

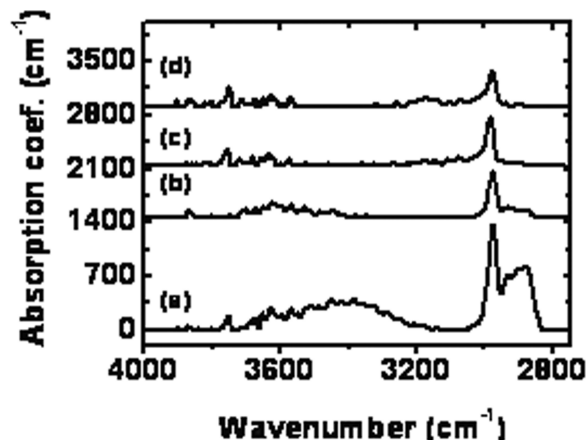


FIG. 3. FTIR absorption spectra of CH<sub>2</sub> and OH region of OS7525 films: (a) as-cured (phase-separated sample after 200 °C curing), (b) SCCO<sub>2</sub> treated at 7000 psi, 200 °C, 14 h, (c) first SCCO<sub>2</sub> treated at 7000 psi, 200 °C, 14 h and then thermally annealed at 430 °C for 2 h, and (d) only thermally annealed at 430 °C for 2 h.

regions under various treatments. Figure 3(a) shows the spectrum for the “as-cured” sample (phase-separated by curing at 200 °C), and Fig. 3(b) is of the same sample treated with SCCO<sub>2</sub> at 7000 psi, 200 °C for 14 h. The pressurized sample shows a significant reduction in the CH stretching band especially the broad shoulder under the CH<sub>3</sub> asymmetric mode. Furthermore, SCCO<sub>2</sub> at 200 °C also reduces the water content in the film considerably. Since the broad shoulder under the CH<sub>3</sub> asymmetric absorption is due only to the presence of PPG, the band reduction is indicative of PPG extraction from the matrix. Other characterization data that will be presented later also support this conclusion. After extraction, the intensity of CH<sub>2</sub> stretching decreases to about 15% of the original band. This translates to a remarkable 85% of PPG extraction in a closed pore morphology assuming that a complete disappearance in CH<sub>2</sub> intensity means no PPG remained in the film. As a control, a fresh sample of as-cured OS7525 was annealed to 200 °C for 14 h in N<sub>2</sub> ambient without SCCO<sub>2</sub> treatment. The result, not shown here, shows no changes in the FTIR spectrum of the films. This confirms that the extraction of PPG was primarily due to SCCO<sub>2</sub> treatment and not from partial thermal decomposition and subsequent volatilization. Figure 3(c) is the spectrum of the sample in Fig. 3(b) (SCCO<sub>2</sub> treated sample) after thermally annealing it to 430 °C for 2 h in N<sub>2</sub> ambient. Figure 3(d) shows the spectrum of a fresh OS7525 film where the PPG is totally removed from the matrix by thermal decomposition at 430 °C for 2 h. The two spectra [Figs. 3(c) and 3(d)] appear similar and the PPG is totally removed from the film.

For the OS4555 film (open-pore interconnected morphology, as shown below), only 8% CH<sub>2</sub> remains in the matrix after SCCO<sub>2</sub> extraction at 7000 psi for 14 h and at

160 °C compared with 15% for the closed-pore morphology after extraction at 200 °C. This is expected because interconnected pores, presumably facilitates SCCO<sub>2</sub> diffusion through the matrix.

Figure 4 shows the absorption spectra in the 1600–400 cm<sup>-1</sup> region of the samples in Fig. 3. This figure shows the changes in the IR spectra as PPG is extracted and also the changes in the Si–O band due to further crosslinking of the matrix under various processing treatments. Figure 4(a) shows the overlapping Si–O and C–O absorption bands of PMSSQ and PPG (1250–980 cm<sup>-1</sup>) for the as-cured sample. As PPG is extracted by SCCO<sub>2</sub>, C–O is removed as shown by a decrease in intensity of the absorption band in Fig. 4(b). As the film in Fig. 4(c) was annealed at 430 °C for complete PPG removal, it crosslinked further via Si–O–Si bridging formation. This is evident from the narrowing of the 1250–980 cm<sup>-1</sup> band and the increase in the absorption at 1045 cm<sup>-1</sup> due to the Si–O bridging bonds. Figure 4(d) shows crosslinked nanoporous PMSSQ film, since complete porogen removal occurs by annealing at 430 °C for 2 h. As expected, the spectra in Figs. 4(c) and 4(d) are almost identical.

## B. Dielectric constant

Table I shows the film thickness, refractive index, dielectric constant and percent porosity of the two samples.

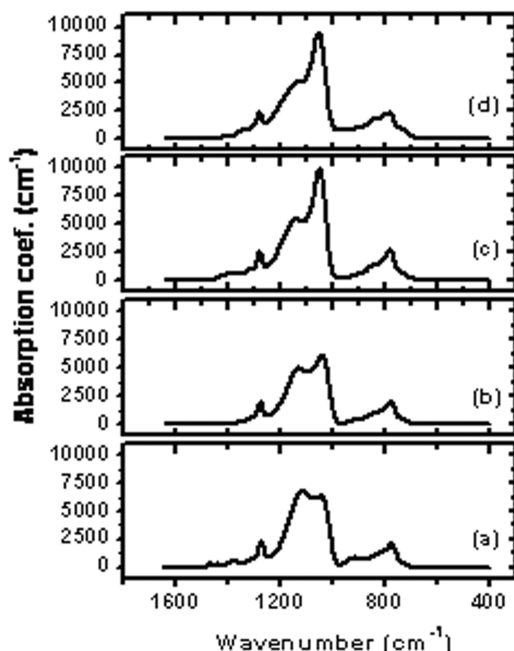


FIG. 4. Si–O FTIR absorption spectra of OS7525 films: (a) as-cured phase-separated sample after 200 °C curing, (b) SCCO<sub>2</sub> treated at 7000 psi, 200 °C, 14 h, (c) first SCCO<sub>2</sub> treated at 7000 psi, 200 °C, 14 h and then thermally annealed at 430 °C for 2 h, and (d) only thermally annealed at 430 °C for 2 h.

The thicknesses of the two as-cured films (OS7525 and OS4555) after SCCO<sub>2</sub> pressurization remain almost constant even though 85% and 92%, respectively, of the porogen have been extracted according to infrared (IR) analysis. This is a very interesting result because it means that the films do not collapse even after significant extraction of the porogen. This is another positive feature of SCCO<sub>2</sub> alone because in many SOD processes, shrinkage or collapse of the pores results in significant stress that may lead to adhesion and delamination problems. However, after thermally annealing the SCCO<sub>2</sub> treated samples to 430 °C for 2 h, the thickness of OS7525 decreased by 22% (from 0.5690 to 0.4435 μm) while that of OS4555 sample decreased by 33% (from 0.9119 to 0.6051 μm). These results are also the same as observed for thermal decomposition of PPG in the films without any SCCO<sub>2</sub> treatment; the thicknesses of the two films decreased by 22% and 31% for OS7525 and OS4555, respectively. Some partial decrease in film thickness may be expected due to matrix condensation and does not indicate pore collapse. As the porogen decomposes, areas with lesser PMSSQ presumably collapse and crosslink to form a more stable structure.<sup>36</sup> The collapse is proportional to the porogen loading; here, the thickness of the sample with 55% porogen loading decreased by 33% while the lower loading of 25% decreased by 22% after complete porogen removal. The refractive indexes of the samples are also shown in the table. After SCCO<sub>2</sub> extraction, the refractive index of OS7525 decreased from 1.44 to 1.31 and OS4555 decreased from 1.44 to 1.15. For the samples annealed at 430 °C after SCCO<sub>2</sub> and for those annealed at 430 °C, the respective refractive indexes are the same, i.e., 1.26 and 1.14 for OS7525 and OS4555, respectively. The dielectric constants of the films are also tabulated and they decrease after SCCO<sub>2</sub> extraction. For the sample with open-pore morphology (OS4555), *k* decreased from 3.1 for pure PMSSQ to 1.87 after SCCO<sub>2</sub> and to 1.47 after SCCO<sub>2</sub> plus thermal annealing. This final value is the same obtained from purely thermal decomposition. For the sample with closed-pore morphology (OS7525), *k* decreased to 2.81 after SCCO<sub>2</sub> and further to 2.29 after SCCO<sub>2</sub> plus annealing. This value is lower than that obtained by thermal decomposition alone (2.47). The decrease in refractive index and dielectric constant is consistent with the removal of PPG and the generation of voids.

## C. Porosity

The volume fraction of porosity is estimated using the Classius–Mossotti equation:

$$V = 1 - \frac{\left[ \frac{(k_p - 1)}{(k_p + 2)} \right]}{\left[ \frac{(k_d - 1)}{(k_d + 2)} \right]}, \quad (1)$$

TABLE I. Thickness, refractive index, dielectric constant, and percent porosity after various treatments of hybrid films.

Sample	Treatment	Thickness <sup>a</sup> (μm)	Refractive index <sup>a,b</sup>	<i>k</i> value ± 0.1	Percent porosity <sup>c</sup>
PMSSQ	PMSSQ film annealed at 200 °C in N <sub>2</sub>	0.4799	1.41	3.10	0
OS7525	As-cured, annealed at 200 °C in N <sub>2</sub>	0.5779	1.44	...	0
	SCCO <sub>2</sub> at 7000 psi 200 °C for 14 h	0.5690	1.31	2.81	...
New OS7525	SCCO <sub>2</sub> + annealed at 430 °C in 600 mTorr N <sub>2</sub> for 4 h	0.4435	1.27	2.29	27.0
	Only annealed at 430 °C in 600 mTorr N <sub>2</sub> for 4 h	0.4502	1.26	2.47	20.1
OS4555	As-cured, annealed at 200 °C in N <sub>2</sub>	0.9205	1.44	...	0
	SCCO <sub>2</sub> at 7000 psi, 160 °C for 14 h	0.9119	1.15	1.87	...
	SCCO <sub>2</sub> + annealed at 430 °C in 600 mTorr N <sub>2</sub> for 4 h	0.6051	1.14	1.47	67.1
New OS4555	Only annealed at 430 °C in 600 mTorr N <sub>2</sub> for 4 h	0.6310	1.14	1.47	67.1

<sup>a</sup><3% dispersion.

<sup>b</sup>Measured by prism coupler.

<sup>c</sup>Calculated using the Classius–Mossoti equation.

where *V* is the relative pore volume, *k<sub>p</sub>* is the dielectric constant for porous material, and *k<sub>d</sub>* is the dielectric constant of the dense matrix (PMSSQ). The calculated porosity of OS7525 after SCCO<sub>2</sub> extraction and thermal annealing is 27% and is larger than observed for the purely annealed sample (20.1%). For the OS4555 sample the porosities are the same (67.1%) for the SCCO<sub>2</sub> extracted and annealed film and the annealed only sample. The porosity of the samples extracted with SCCO<sub>2</sub> alone cannot be estimated using this equation due to the residual PPG component that affects *k<sub>p</sub>*. A plot of *k* versus the porosity for PMSSQ is shown in Fig. 5. The plot is modeled from the Bruggemann effective medium approximation (BEMA) considering a two-component film composed of thermally annealed PMSSQ at 430 °C (*k* = 2.85) and air (*k* = 1.0).<sup>31</sup> The plot shows increasing porosity with decreasing dielectric constant. The calculated percent porosity after SCCO<sub>2</sub> extraction followed by thermal annealing for both OS7525 and OS4555

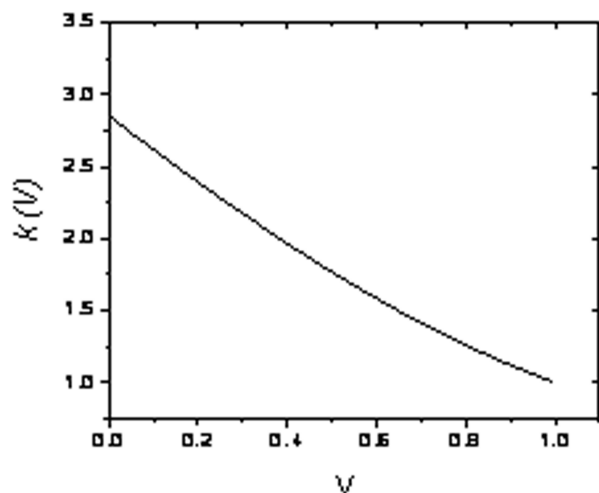


FIG. 5. Bruggeman effective medium approximation of a two-component film of a 430 °C annealed PMSSQ (*k* = 2.85) and air (*k* = 1).

samples correlates well with the curve. For *k* = 2.29, the corresponding porosity is expected to be 25% (BEMA) compared with 27% in our calculation for OS7525, while for *k* = 1.47 the porosity is 67% (BEMA), which is the same with our calculation for OS4555.

#### D. Small-angle x-ray scattering

Small-angle x-ray scattering (SAXS) was used to verify the porous structure. Figure 6(a) shows the background subtracted, circularly averaged, and transmitted beam intensity normalized SAXS profiles. The open and closed symbols correspond to the porous films prepared by SCCO<sub>2</sub> treatment at 200 °C and by only the thermal method (430 °C), respectively. Here the scattering vector is *q* = (4π/λ)sin(θ/2), where λ and θ are the x-ray wavelength and the scattering angle, respectively. For both pore-generation methods, the scattering intensity increases and with increasing porogen loading the *q* where the intensity sharply drops shifts to smaller values. Since the *q* value where the intensity drops is approximately equal to π/2*r*, where *r* is the average radius of the pores, this shows that the average pore size increases with increased loading. To determine the pore distribution, we have quantitatively modeled the SAXS data as described in Ref. 27. The scattered intensity *I*(*q*) is

$$I = c \int_0^\infty n(r) f(qr) S(qr) dr \quad , \quad (2)$$

where *c* is a constant, *n*(*r*) is the pore-size distribution, *f*(*qr*) is the spherical form factor, and *S*(*qr*) is the structure factor for the hard sphere model using the local monodisperse approximation from Pedersen.<sup>37</sup> The best fits to the data were obtained using log-normal pore-size distributions and are shown by the solid lines in Fig. 6(a). They fit the data well, except at the lowest *q* where slit scattering contributes to the observed intensity. The best-fit pore-size distributions are shown in Fig. 6(b); these show that the average pore size increases and the size

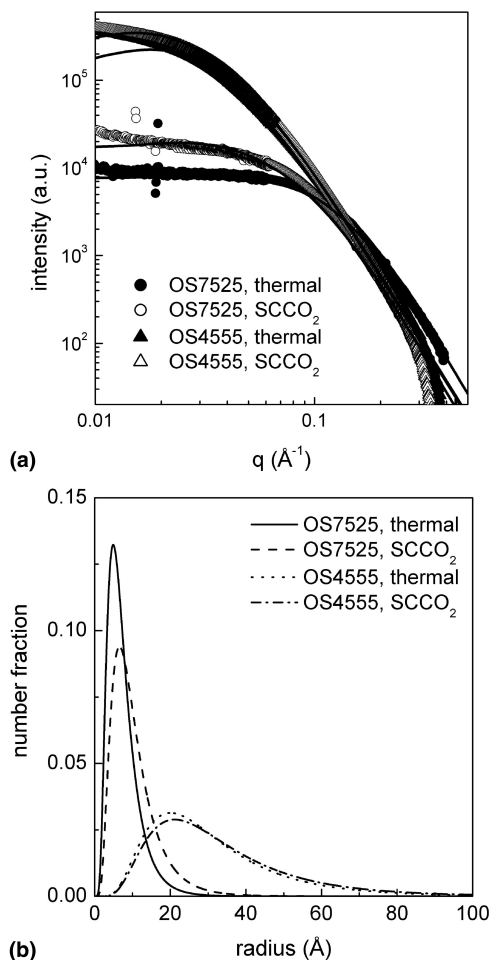


FIG. 6. SAXS profiles of nanoporous PMSSQ: (a) closed and open symbols present thermal and SCCO<sub>2</sub> processes, respectively; (b) pore-size distribution obtained from the best fits [solid lines in (a)].

distribution broadens with increasing initial PPG content and, hence, with increasing porosity. It is noted that both pore generation methods give similar porosities and pore-size distributions for OS4555, whereas for OS7525 the SCCO<sub>2</sub> process gives broader size distribution than thermal method. As suggested before,<sup>25</sup> this analysis approach employing a spherical model is questionable for films where the pores become interconnected, the 55% loading level films. Therefore, we have also analyzed the SAXS data using a method suited to films with interconnected pores<sup>38</sup> with results described below.

### E. Representative pore morphology

Representative 3-dimensional pore morphologies were generated from SAXS data using an analysis method<sup>38</sup> that builds on work by Cahn,<sup>39</sup> Berk,<sup>32,38,40</sup> and others.<sup>41–45</sup> While the morphologies are only representative (i.e., not a reconstruction), they do statistically reproduce the pore morphology. The major assumption of this approach is that the two-phase morphology (pore and matrix) is

isotropic and sufficiently disordered. Specifically, the morphology can be described by a sum of sinusoidal waves with random orientation and phase, where the wave amplitudes come directly from the SAXS data. Previously, this modeling approach has been used to analyze SAXS and small-angle-neutron-scattering (SANS) data for isometric cases where both phases have equal volume fractions.<sup>41–45</sup> Choy and Chen<sup>44</sup> have used the method for non-isometric microemulsions, but did not directly use their SANS data to produce the microemulsion morphology.

The pore morphology is generated from a Gaussian random function  $[\Psi(r)]$ ; this is where the assumption of disorder appears. First, the SAXS data  $I(q)$  are extrapolated to high  $q$  as  $q^{-4}$ . Although this is not necessary, it prevents ringing in subsequent steps. The  $I(q)$  is then Fourier transformed to produce the Debye correlation function  $\Gamma^\alpha(r)$

$$\Gamma^\alpha(r) = \int_0^\infty 4\pi q^2 I(q) [\sin(qr)/(qr)] dq \quad , \quad (3)$$

where  $r$  represents real space,  $\alpha$  is the clipping parameter, which is related to the porosity, and this function is normalized such that  $\Gamma^\alpha(\infty) = [\Gamma^\alpha(0)]^2$ . The Debye correlation function is related to the correlation function  $g(r)$  of  $\Psi(r)$  by<sup>46</sup>

$$\Gamma^\alpha(r) = \Gamma^\alpha(0) - \left(\frac{1}{2\pi}\right) \int_{g(r)}^1 \frac{\exp[-\alpha^2/(1+t)]}{\sqrt{1-t^2}} dt \quad , \quad (4)$$

where  $\Gamma^\alpha(0)$  is the volume fraction of one of the phases (e.g., the porosity) and, hence, is known. It is related to the clipping parameter  $\alpha$  by

$$\Gamma^\alpha(0) = \frac{1}{\sqrt{2\pi}} \int_\alpha^\infty \exp[-x^2/2] dx \quad . \quad (5)$$

Equations (3)–(5) permit determination of both  $\alpha$  and  $g(r)$  from the known porosity and SAXS data. The spectral function  $f(k)$  of the Gaussian random function  $\Psi(r)$  is then obtained by the inverse Fourier transform of  $g(r)$ :

$$f(k) = \int_0^\infty 4\pi r^2 g(r) [\sin(kr)/(kr)] dr \quad . \quad (6)$$

Hence,  $f(k)$  is obtained from the experimental data with no a priori assumptions about its functional form. The Gaussian random function  $\Psi(r)$  is generated by summing many ( $N = 10,000$ ) sinusoidal waves

$$\Psi(r) = \sqrt{\frac{2}{N}} \sum_{i=1}^N \cos(k_i \cdot r + \phi_i) \quad , \quad (7)$$

where the directions of wavevectors  $k_i$  and phases  $\phi_i$  are random, but the magnitudes of wavevectors  $k_i$  are obtained from the spectral function given by Eq. (6). To obtain the two-phase morphologies, the field is then

clipped to the corresponding  $\alpha$  calculated in Eq. (5). In other words, all points  $r$  with  $\Psi(r) > \alpha$  are assigned to one phase and all other points are assigned to the other phase.

Figure 7 shows representative morphologies for different porogen loadings for a 200 nm cube obtained using the method described above. Gray and black correspond to the PMSSQ matrix, respectively, and the pore interior as seen through the cube side. As shown in Fig. 7, the average pore size increases as the loading increases for porous films prepared by both thermal decomposition and supercritical CO<sub>2</sub> (SCF in figures) extraction. Although it would be quite valuable to estimate the average pore sizes obtained from this method, for 55% loading, the morphology becomes bi-continuous (see below) and one can not easily define an average pore size.

Figure 8 presents another visualization of the pore morphology that permits determination of the extent of pore interconnection. The PMSSQ matrix is transparent and the pores are shown as seen from outside the cube. The largest pore is colored black for the cubes on the largest left side, and this pore is removed on the right side of the figure. For 55% porogen loadings, the elimination of the largest pore results in the removal of most of the pore volume. This shows that at 55% loading the pore morphologies are bi-continuous for both pore generation methods. Moreover, at 25% loading, Fig. 8 demonstrates that while morphologies are somewhat interconnected, they are not bi-continuous.

#### IV. SUMMARY

Supercritical CO<sub>2</sub> extraction of PPG in phase-separated nanohybrid films has been achieved for both

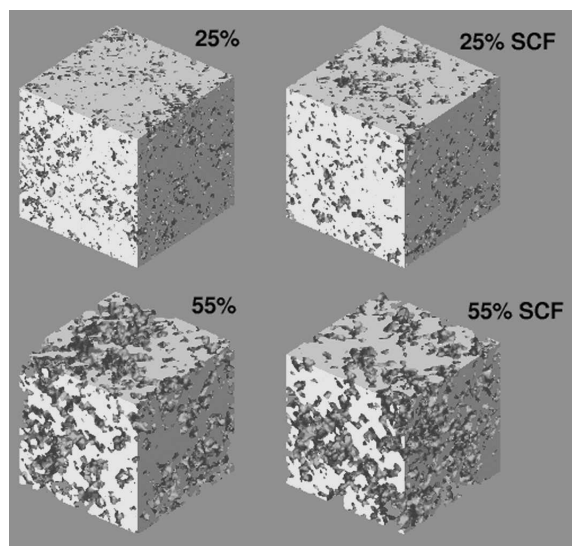


FIG. 7. Visualization of representative microstructures for 200 nm cubes. Gray and black correspond to the PMSSQ matrix and the pore interior as seen through the cube side, respectively.

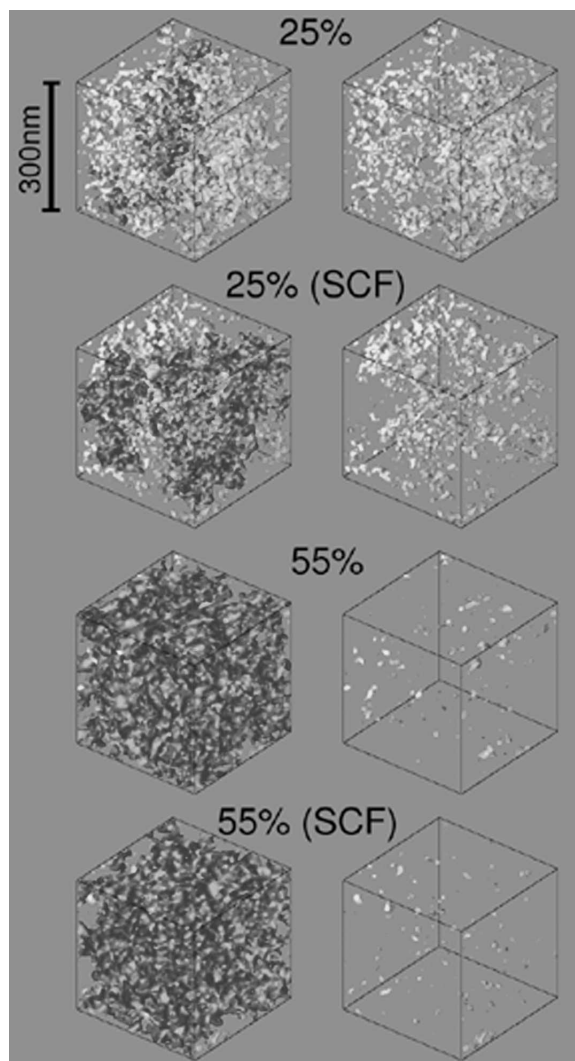


FIG. 8. Images of microstructures for a cube side of 300 nm. The PMSSQ matrix is transparent and the pores are seen from the outside of the cube side. On the left, the largest pore is shown in black, while this is removed on the right side.

closed- and open-pore morphology structures. Extraction of over 85% CH<sub>2</sub> is accomplished without change in thickness of the films. These extractions were performed at much lower temperatures <200 °C compared with thermal decomposition, which was done at 430 °C. Interestingly, porogen extraction is achieved even at low porogen loading levels where the film morphology is largely dispersed. Subsequent thermal treatment of the samples leads to further decreases in both the dielectric constant and refractive index. SAXS measurements on the samples show the presence of pores and are analyzed to construct representative 3-dimensional pore morphologies. Decreases in refractive indices and dielectric constants validate the presence of pores and show significant decrease in density. SCCO<sub>2</sub> is a very promising tool in the fabrication of nanoporous films. We believe



that optimization of treatment conditions, addition of proper solvent or co-solvent and using dynamic mode of extraction will enhance removal efficiency and decreased process times.

## ACKNOWLEDGMENTS

Professor Gangopadhyay and Professor Simon acknowledge the financial support of this work from the Semiconductor Research Corporation and from the National Science Foundation Grant No. CMS-0210230. The authors would also like to acknowledge initial support provided by the State of Texas Advanced Technology Program (ATP Grant No. 003644-0229-1999). The SAXS experiments were performed at the Advanced Photon Source at Argonne National Laboratory, which is supported by the United States Department of Energy, Office of Science, Office of Basic Energy Sciences, under Contract No. W-31-109-ENG-38. Portions of this research were carried out at the Stanford Synchrotron Radiation Laboratory, a national user facility operated by Stanford University on behalf of the United States Department of Energy, Office of Basic Energy Sciences

## REFERENCES

1. W. Lee and P. Ho: Low-dielectric constant materials. *MRS Bull.* **22**, 10 (1997), pp. 19–23.
2. <http://www.intel.com/research/silicon/mooreslaw.htm>. Jan. 2004.
3. J.H. Golden, C.J. Hawker, and P.S. Ho: Designing porous low-k dielectrics. *Semicond. Int.* **24**, 79 (2001).
4. <http://public.itrs.net>. Sept. 2004.
5. S. Polarz and B. Smarsly: Nanoporous materials. *J. Nanosci. Nanotech.* **2**, 581 (2002).
6. M.D. Loque de Castro, M. Valcarcel, and M.T. Tena: *Analytical Supercritical Fluid Extraction* (Springer-Verlag, Berlin Heidelberg, Germany, 1994), p. 67.
7. Los Alamos Newsletter, Vol 2, No 3, Feb. 8, 2001, “SCORR scores big,” K. Roa. edited by K. Delucas, pp. 1–2.
8. M.A. Biberger, P. Schilling, D. Frye, and E. Mills: *Semiconductor FabTech* 12th ed., (Henry Publishing Ltd., London, U.K.), pp. 239–243.
9. S. Ogawa, T. Nasuno, M. Egami, and A. Nakashima: Formation of Mechanically Strong Low-k Film using Supercritical Fluid Dry Technology, in International Interconnect Technology Conference, June 3–5, 2002. (Omni Press, Madison, WI).
10. J.A. Lubguban, J. Sun, T. Rajagopalan, B. Lahlouh, S.L. Simon, and S. Gangopadhyay: Supercritical carbon dioxide extraction to produce low-k plasma enhanced chemical vapor deposited dielectric films. *Appl. Phys. Lett.* **81**, 4407 (2002).
11. G. Madras, C. Erkey, and A. Akgerman: Supercritical extraction of organic contaminants from soil combined with adsorption onto activated carbon. *Environ. Prog.* **13**, 45 (1994).
12. G. Madras, C. Thibaud, C. Erkey, and A. Akgerman: Modeling of supercritical extraction of organics from solid matrices. *AIChE J.* **40**, 777 (1994).
13. D. Barth, D. Chouchi, G.D. Porta, E. Reverchon, and M. Perrut: Desorption of lemon peel oil by supercritical carbon-dioxide—Deterpenation and psoralens elimination. *J. Supercrit. Fluids* **7**, 177 (1994).
14. E. Reverchon, L.S. Osseo, and D. Gorgoglione: Supercritical CO<sub>2</sub> extraction of basil oil—Characterization of products and process modeling. *J. Supercrit. Fluids* **7**, 185 (1994).
15. M. Sato, M. Goto, and T. Hirose: Fractional extraction with supercritical carbon-dioxide for the removal of terpenes from citrus oil. *Ind. Eng. Chem. Res.* **34**, 3941 (1995).
16. M. Sato, M. Goto, and T. Hirose: Supercritical fluid extraction on semibatch mode for the removal of terpene in citrus oil. *Ind. Eng. Chem. Res.* **35**, 1906 (1996).
17. J. Beckman: Carbon dioxide extraction of biomolecules. *Science* **271**, 613 (1996).
18. K.E. Laintz, J.J. Yu, and C.M. Wai: Separation of metal-ions with sodium bis(trifluoroethyl)dithiocarbamate chelation and supercritical fluid chromatography. *Anal. Chem.* **64**, 311 (1992).
19. K.E. Laintz, C.M. Wai, C.R. Yonker, and R.D. Smith: Extraction of metal-ions from liquid and solid materials by supercritical carbon dioxide. *Anal. Chem.* **64**, 2875 (1992).
20. S.F. Wang, S. Elshani, and C.M. Wai: Selective extraction of mercury with ionizable crown-ethers in supercritical carbon-dioxide. *Anal. Chem.* **67**, 919 (1995).
21. J.M. Murphy and C. Erkey: Thermodynamics of extraction of copper (II) from aqueous solutions by chelation in supercritical carbon dioxide. *Environ. Sci. Technol.* **31**, 1674 (1997).
22. R.E. Zacharia, S.L. Simon, E.J. Beckman, and R.M. Enick: Improving the thermal stability of a polymer through liquid carbon dioxide extraction of a transition metal catalyst. *Journal Polym. Degrad. Stability* **63**, 85 (1999).
23. B. Lahlouh, T. Rajagopalan, J.A. Lubguban, N. Biswas, S. Gangopadhyay, J. Sun, D. Huang, S.L. Simon, H.C. Kim, W. Volksen, and R.D. Miller: Creating nanoporosity by selective extraction of porogens using supercritical carbon dioxide/co-solvent processes, in *Materials, Technology and Reliability for Advanced Interconnects and Low-k Dielectrics—2003*, edited by A.J. McKerrow, J. Leu, O. Kraft, and T. Kikkawa (Mater. Res. Soc. Symp. Proc. **766**, Warrendale, PA, 2003), p. 291.
24. T. Rajagopalan, B. Lahlouh, J.A. Lubguban, N. Biswas, S. Gangopadhyay, J. Sun, D.H. Huang, S.L. Simon, A. Mallikarjunan, H.C. Kim, W. Volksen, M.F. Toney, E. Huang, P.M. Rice, E. Delenia, and R.D. Miller: Supercritical carbon dioxide extraction of porogens for the preparation of ultralow dielectric constant films. *Appl. Phys. Lett.* **82**, 4328 (2003).
25. E. Huang, M.F. Toney, W. Volksen, D. Mecerreyes, P. Brock, H.C. Kim, C.J. Hawker, J.L. Hedrick, V.Y. Lee, T. Magbitang, R.D. Miller, and L.B. Lurio: Pore-size distributions in nanoporous methyl silsesquioxane films as determined by small angle x-ray scattering. *Appl. Phys. Lett.* **81**, 2232 (2002).
26. R.H. Baney, M. Itoh, A. Sakakibara, and T. Suzuki: Silsesquioxanes. *Chem. Rev.* **95**, 1409 (1995).
27. G.Y. Yang, R.M. Briber, E. Huang, P.M. Rice, W. Volksen, and R.D. Miller: Formation and characterization of nanoporous ultralow dielectric materials using TEM and SANS Proceedings of the ACS. *Polym. Mater. Sci. Eng.* **85**, 18 (2001).
28. R.D. Miller, J.L. Hedrick, D.Y. Yoon, R.F. Cook, and J.P. Hummel: Phase-separated inorganic-organic hybrids for microelectronic applications. *MRS Bull.* **22**, 44 (1997).
29. J.L. Hedrick, S. Srinivasan, H-J. Cha, D. Yoon, V. Flores, M. Harbison, R. Di Pietro, W. Hinsberg, V. Deline, H.R. Brown, M. Sherwood, E. Paulson, R.D. Miller, R. Cook, E. Liniger, E. Simonyi, D. Klaus, S. Cohen, and J. Hummel: Toughened inorganic-organic hybrid materials for microelectronic application, in *Low-Dielectric Constant Materials II*, edited by A. Lagendijk, H. Treichel, K.J. Uram, and A.C. Jones (Mater. Res. Soc. Symp. Proc., San Francisco, CA, **443**, 1997) pp. 47–58.
30. C.V. Nguyen, C.J. Hawker, J.L. Hedrick, R.L. Jaffe, R.D. Miller, J.F. Remenar, H-W. Rhee, M.F. Toney, M. Trollsas, W. Volksen,

- and D.Y. Yoon: Structure-property relationships for nano-porous poly(methyl-silsesquioxane) films with low-dielectric constants prepared via organic/inorganic polymer hybrids. *Electrochem. Soc. Proc.* **99**, 38 (1999).
31. M. Kiene, M. Morgen, J. Zhao, C. Hu, T. Cho, and P. Ho: Characterization of low-dielectric constant materials, in *Handbook of Silicon Semiconductor Metrology*, edited by A.C. Diebold (Marcel Dekker, New York, 2001), p. 265.
  32. N.F. Berk: Scattering properties of the leveled-wave model of random morphologies. *Phys. Rev. A* **44**, 5069 (1991).
  33. J.A. Lubguban, T. Rajagopalan, N. Mehta, B. Lahlouh, S.L. Simon, and S. Gangopadhyay: Low-k organosilicate films prepared by tetravinyltetramethylcyclotetrasiloxane. *J. Appl. Phys.* **92**, 1033 (2002).
  34. C. Rau and W. Kulisch: Mechanisms of plasma polymerization of various silico-organic monomers. *Thin Solid Films* **249**, 28 (1994).
  35. G. Socrates: *Infrared Characteristics Group Frequencies* (Wiley, New York, 1994), Chap. 18.
  36. R.D. Miller, W. Volksen, V. Lee, T. Magbitang, L. Sundberg, H.-C. Kim, C.J. Hawker, and J.L. Hendrick, International Sema-tech Ultra Low k Workshop, June 6–7, San Francisco, CA, 2002.
  37. J.S. Pedersen: Determination of size distribution from small-angle scattering data for systems with effective hard-sphere interactions. *J. Appl. Crystallogr.* **27**, 595 (1994).
  38. J.A. Hedstrom, M.F. Toney, E. Huang, H.-C. Kim, W. Volksen, T. Magbitang, and R.D. Miller: Pore morphologies in disordered nanoporous thin films. *Langmuir* **20**, 1535 (2004).
  39. J.W. Cahn: Phase separation by spinodal decomposition in isotropic systems. *J. Chem. Phys.* **42**, 93 (1965).
  40. N.F. Berk: Scattering properties of a model bicontinuous structure with a well defined length scale. *Phys. Rev. Lett.* **58**, 2718 (1987).
  41. H. Jinnai, Y. Nishikawa, S.-H. Chen, S. Koizumi, and T. Hashimoto: Morphological characterization of bicontinuous structures in polymer blends and microemulsions by the inverse-clipping method in the context of the clipped-random-wave model. *Phys. Rev. E* **61**, 6773 (2000).
  42. D. Choy and S.-H. Chen: Clipped random wave analysis of isometric lamellar microemulsions. *Phys. Rev. E* **61**, 4148 (2000).
  43. M. Teubner: Level surfaces of gaussian random fields and microemulsions. *Europhys. Lett.* **14**, 403 (1991).
  44. D. Choy and S.-H. Chen: Clipped random wave analysis of anisometric lamellar microemulsions. *Phys. Rev. E* **63**, 021401 (2001).
  45. A.P. Roberts: Statistical reconstruction of three-dimensional porous media from two-dimensional images. *Phys. Rev. E* **56**, 3203 (1997).
  46. S.-H. Chen and S.-L. Chang: Simulation of bicontinuous microemulsions: Comparison of simulated real-space microstructures with scattering experiments. *J. Appl. Crystallogr.* **24**, 721 (1991).